International Symposium
On Turbulence and Shear Flow
Phenomena (TSFP-9)
June 30 - July 3, 2015 *Melbourne, Australia*

QUANTITATIVE MEASUREMENTS OF ABLATION-PRODUCTS TRANSPORT IN A SUPERSONIC TURBULENT BOUNDARY LAYER USING SIMULTANEOUS PIV AND NAPHTHALENE PLIF

Christopher S. Combs
Department of Aerospace Engineering and Engineering Mechanics
The University of Texas at Austin
210 E. 24th St., Austin, Texas, 78712, United States
ccombs0022@gmail.com

Noel T. Clemens
Department of Aerospace Engineering and Engineering Mechanics
The University of Texas at Austin
210 E. 24th St., Austin, Texas, 78712, United States
clemens@mail.utexas.edu

ABSTRACT

The dispersion of a passive scalar in a Mach 5 turbulent boundary layer is investigated using a low-temperature sublimating ablator (naphthalene). Two-dimensional fields of naphthalene mole fraction and velocity are obtained by using simultaneous particle image velocimetry (PIV) and planar laser-induced fluorescence (PLIF). The images show large-scale naphthalene vapor structures that coincide with regions of relatively low streamwise velocity. Additionally, the covariance of naphthalene mole fraction with velocity indicates that an ejection mechanism is transporting low-momentum, high-scalar-concentration fluid away from the wall, resulting in the protrusions of naphthalene vapor evident in the instantaneous PLIF images. Mean profiles of streamwise velocity and naphthalene mole fraction are also presented, with the mean mole fraction profile having the expected shape of a classical scalar boundary layer profile.

INTRODUCTION

There remains continued interest in the study of ablation owing to the need to develop suitable thermal protection systems (TPS) for spacecraft that undergo planetary entry. Charring ablation experienced during atmospheric entry is a complex process involving heat and mass transfer, and codes that predict it require a number of coupled submodels, each of which requires validation (Smits et al., 2009). For example, Reynolds-averaged Navier-Stokes (RANS) and large-eddy simulation (LES) codes require models of the turbulent transport of ablation products; however, suitable scalar-velocity data under relevant conditions are very rare (Ho et al., 2007). Additioanlly, Stogner et al. (2011) conducted an uncertainty analysis of ablation calculations and concluded that turbulence models are one of the largest contributors to the uncertainty of ablation predictions for re-entry flows. A technique has been under development at The University of Texas at Austin that uses planar laser-induced fluorescence (PLIF) of a low-temperature sublimating ablator (naphthalene) to enable visualization of the ablation products in a hypersonic flow (Lochman, 2010; Buxton et al., 2012; Combs et al., 2014a; Combs et al., 2014b; Combs and Clemens, 2015).

Lochman (2010) first used naphthalene PLIF to study the transport of ablation products in a Mach 5 turbulent boundary layer. In his work, the technique provided images of naphthalene vapor in the turbulent boundary layer with excellent signal-to-noise ratio (SNR), visualizing both large and small-scale turbulent structures. However, while some spectroscopic measurements were made, a temperature correction was only applied to the profile of the naphthalene boundary layer to yield a "corrected" profile and the images presented are qualitative visualizations. Additionally, no velocity data was collected. In the work by Buxton et al. (2012), naphthalene PLIF was performed simultaneously with particle image velocimetry (PIV) in a Mach 5 turbulent boundary layer using the same insert design as Lochman, providing scalar-velocity data of ablation-products transport in the boundary layer. Mean and instantaneous boundary layer profiles of velocity, RMS velocity, and fluorescence signal were determined. The results indicated that there was a strong correlation of high fluorescence signal with negative streamwise and positive spanwise velocity fluctuations away from the wall. However, naphthalene concentration was not determined from the PLIF images since the PLIF signals were not corrected for temperature effects and the PLIF images had a low SNR. Combs et al. (2014a, 2014b) used naphthalene PLIF to image ablation-products transport from the heat shield of an Orion Multi-Purpose Crew Vehicle (MPCV) model in a Mach 5 flow. Still, these images were purely qualitative flow visualizations with no attempt made to correct the PLIF signal for temperature and pressure effects and no velocity data was collected. Most recently, Combs and

Clemens (2015) collected quantitative naphthalene PLIF measurements in a Mach 5 turbulent boundary layer. Employing spectroscopic measurements made in a flowing test cell, the naphthalene PLIF signal was converted into mole fraction with an uncertainty of ± 20%. The images revealed large-scale naphthalene vapor structures in the turbulent boundary layer with naphthalene mole fraction of approximately 1% of the saturation mole fraction at the temperature and pressure conditions present in the boundary layer. The mean profile of mole fraction in the boundary layer was presented as well (Combs and Clemens, 2015). While this work used spectroscopic data to compute naphthalene mole fraction, no velocity measurements were made.

In the current work, simultaneous naphthalene PLIF and PIV are used to obtain quantitative scalar-velocity data on the turbulent transport of ablation products in a Mach 5 turbulent boundary layer. As in the work by Lochman (2010), Buxton et al. (2012), and Combs and Clemens (2015), the naphthalene vapor is introduced into the flow by sublimation from a naphthalene flush-mounted floor insert. Empirical relationships for naphthalene fluorescence signal and yield developed by Combs and Clemens (2015) are employed in the current work. Assuming constant static pressure across the boundary layer, and using the mean temperature derived from the Crocco-Busemann relation, instantaneous measurements of naphthalene mole fraction were estimated to have ±15% uncertainty (Combs and Clemens, 2015). When combined with simultaneously-acquired PIV data, these data permit analysis of scalar-velocity correlations in the Mach 5 turbulent boundary layer.

EXPERIMENTAL PROGRAM

Wind Tunnel Facility

The facility used for these experiments was a low-enthalpy blow-down Mach 5 wind tunnel. The wind tunnel was supplied by a 4 m^3 storage tank held at approximately 15.5 MPa and the plenum pressure was maintained at approximately 2.5 MPa ± 15 kPa. The flow was electrically heated to achieve a stagnation temperature of about 360 K ± 4 K. The test section of the facility has a constant cross-section and is 152 mm wide by 178 mm tall. The freestream and boundary layer conditions were fully characterized in previous work by McClure (1992), with a freestream unit Reynolds number, Re, of 57.2×10^6 m^{-1} and freestream velocity of 770 m/s. Boundary layer transition occurred naturally upstream of the test section so that the incoming boundary layer was fully developed and fully turbulent with a boundary layer thickness, δ_{99}, of 19.3 mm, a momentum thickness, θ, of 0.76 mm and $Re_\theta = 4.4\times10^4$. Optical access for laser transmission and imaging was provided by fused silica windows on the wind tunnel floor, ceiling, and sidewall.

In these experiments, the naphthalene vapor was introduced into the flow by sublimation of a solid naphthalene insert (105 mm long × 57 mm wide) that was mounted to the floor of the wind tunnel. The solid block of naphthalene, depicted in Figure 1, was formed by pouring liquid naphthalene into a mold and then covering it during the cooling process to ensure a smooth, flush surface. After the naphthalene solidified, the cover was removed and the insert was installed into the test section floor. The sublimation rate of naphthalene at standard conditions is slow and no noticeable mass was lost if the insert was left in the test section for hours without flow. Only a small amount of ablation (less than a fraction of a millimeter) was observed over the course of a one minute wind tunnel run.

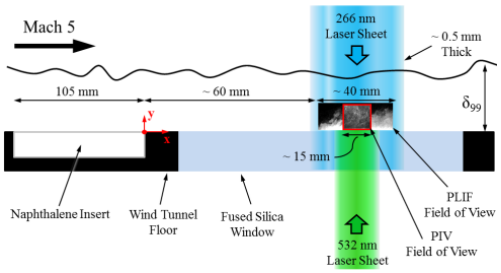

Figure 1. Schematic of the naphthalene insert and imaging field of view. The coordinate system employed is indicated by the red axes.

PLIF Experimental Setup

The naphthalene vapor was excited by a sheet of 266 nm light from a frequency-quadrupled Nd:YAG laser (Spectra-Physics Quanta-Ray GCR-150)—depicted in Figure 2—operating at a rate of 10 Hz. The laser energy was maintained at approximately 42 mJ/pulse, corresponding to an irradiance of 150 kW/mm^2. The UV laser beam was oriented by a series of laser mirrors so that it passed up to the top of the wind tunnel facility where it was formed into a laser sheet using a 250 mm spherical lens and a 25 mm cylindrical lens and transmitted through the test section, as seen in Figure 2. The resulting laser sheet was about 0.5 mm thick (FWHM) in the measurement region and approximately 50 mm wide. PLIF images were recorded using a back-illuminated high-UV quantum efficiency CCD camera (Apogee Alta F47, 1024×1024) fitted with a 100 mm focal length, f/2.8 UV lens (Circo) operated at full aperture. In order to reject scattered laser light and image only naphthalene fluorescence, one Schott WG-295 filter and one Schott UG-11 filter were placed in front of the camera. The imaging field of view was approximately 40 mm wide by 16 mm tall. The images were obtained at a rate of approximately 1/3 Hz with a 90 millisecond exposure time and as many as 30 images could be acquired per wind tunnel run. The coordinate system applied to the PLIF and PIV fields of view is as follows: the *x*-direction is aligned with the freestream while the *y*-direction is normal to the wind tunnel floor, with the origin located at the trailing edge of the naphthalene insert and on the same plane as the laser sheet, as illustrated in Figure 1. The experiment was synchronized using three Stanford Research Systems digital delay generators to ensure that images were acquired while the laser was firing.

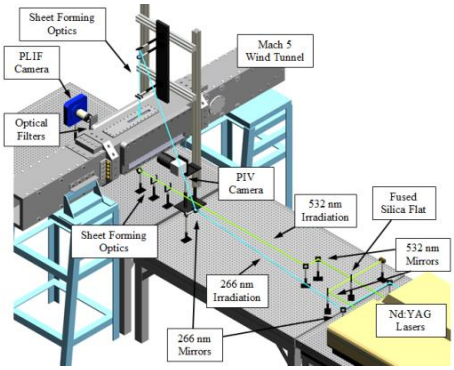

Figure 2. Simultaneous PIV/PLIF Setup.

PIV Experimental Setup

Titanium Dioxide (TiO_2) was used as the seed particle for PIV. The particles were seeded via a two-stage fluidized bed driven by compressed air into a cyclone separator system and injected directly into the boundary layer of the lower wall, just upstream of the convergent section of the wind tunnel nozzle. Hou (2003) studied particle seeding in the wind tunnel used for the present work and measured the nominal particle diameter to be approximately 0.26 μm and calculated the particle response time to be 2.9 μs. This results in a particle Stokes number of 0.11 for the Mach 5 boundary layer conditions, satisfying the guideline established by Samimy and Lele (1991) of a particle Stokes number < 0.5 for reliable flow tracking.

The seed particles were illuminated by two sheets of 532 nm irradiation from frequency-doubled Nd:YAG lasers and imaged using a high-speed CCD camera (Princeton Instruments MegaPlus ES4020, 2048x2048), as seen in Figure 2. The camera was equipped with a Nikkor 105 mm macro lens operated at an aperture of f/5.6, which resulted in a field of view of approximately 16x16 mm.

The first laser sheet was generated by the residual 532 nm light from the GCR-150 laser used for PLIF excitation and was thus syncronized with the PLIF image. A single cavity from a Spectra-Physics Quanta-Ray PIV-400 laser was used to generate the second laser sheet and was delayed by 250 ns relative to the GCR-150. As shown in Figure 2, the laser pulses were combined using an uncoated fused silica flat. The GCR-150 beam passed through the fused silica flat and combined with the approximately 10% reflection from the PIV-400 beam that was incident to the flat 90° relative to the GCR-150 beam. This resulted in two coincident beams with pulse energies of approximately 15 mJ/pulse each.

The light sheets formed for PIV and PLIF were then aligned so that they were coincident and the two fields of view overlap, as illustrated in Figure 1.

PLIF Image Processing

Single-shot PLIF images were processed in MATLAB by first removing the background and then were corrected for variations in the mean intensity profile of the laser sheet. Single-shot sheet corrections were not made. The mean laser sheet spatial intensity variation was measured by imaging the mean fluorescence of naphthalene vapor present in the test section prior to a run with the same CCD camera used for the PLIF experiments. Instantaneous images of naphthalene vapor in quiescent air were visualized as large, uniform streaks of fluorescence signal. Upon averaging approximately 20 of these images a uniform two-dimensional laser sheet profile was observed. The single-shot images obtained during the runs were then divided by this laser-sheet intensity profile to correct for spatial variations in laser energy.

Additionally, a room temperature reference cell saturated with naphthalene vapor was pulled to a vacuum (4.92 kPa ± 10 Pa), placed in the Mach 5 test section in the path of the 266 nm laser sheet, and imaged to generate reference images for quantifying the fluorescence signal. These images were also corrected for variations in laser sheet intensity by using the same technique described above. The naphthalene reference cell was not used for making sheet corrections of the wind tunnel images because the cell could not be oriented in a way that permitted imaging the same field of view.

After correcting the images for non-uniformities in the laser sheet the measured fluorescence signal and reference fluorescence signal were input into Eq. 1:

$$\chi_i = \chi_{i,ref} \frac{S_f}{S_{f,ref}} \frac{P_{ref}T}{PT_{ref}} \frac{\sigma_a(T_{ref})}{\sigma_a(T)} \frac{\varphi(T_{ref},P_{ref},\chi_{ref})}{\varphi(T,P,\chi)} \qquad (1)$$

where χ_i is the species mole fraction, S_f is fluorescence signal, σ_a is the absorption cross section, φ is the fluorescence yield, P is pressure, T is temperature, and the subscript *ref* denotes a known reference condition.

This equation requires input in the form of relationships for absorption cross section and fluorescence yield to solve for naphthalene mole fraction. In the current work, these fits were taken from Combs and Clemens (2015). The fit equations are presented as Equations 2 and 3 while the corresponding coefficients are provided in Tables 1 and 2.

$$\frac{\varphi(T,P)}{\varphi(T_{ref},P_{ref})} = \frac{1}{C_1P+C_2} \Big/ \frac{1}{D_1P_{ref}+D_2} \qquad (2)$$

where $C_i = a_{i1}T^2 + a_{i2}T + a_{i3}$ *and* $D_i = a_{i1}{T_{ref}}^2 + a_{i2}T_{ref} + a_{i3}$.

Table 1. Measured coefficients in Equation 2 from Combs and Clemens (2015).

a_{11}	7.77 ×10^{-8} 1/kPa/K^2	a_{21}	-4.12 × 10^{-8} 1/K^2
a_{12}	-7.57 × 10^{-5} 1/kPa/K	a_{22}	8.40 × 10^{-5} 1/K
a_{13}	2.41 × 10^{-2} 1/kPa	a_{23}	-2.61 × 10^{-3}

$$\frac{\sigma_a(T)}{\sigma_a(T_{ref})} = \frac{S_f(T)}{S_{f,ref}(T_{ref})} \sqrt{\frac{T}{T_{ref}}} \frac{\sigma_{q,O_2}(T)}{\sigma_{q,O_2}(T_{ref})} \qquad (3)$$

where $S_f(T) = b_1T^3 + b_2T^2 + b_3T + b_4$ and $\sigma_{q,O_2}(T) = c_1T + c_2$ = oxygen quenching cross-section..

Table 2. Measured coefficients in Equation 3 from Combs and Clemens (2015).

b_1	-8.72×10^{-9} 1/K^3	c_1	-3.88×10^{-22} 1/K
b_2	1.88×10^{-6} 1/K^2	c_2	4.57×10^{-19}
b_3	3.56×10^{-3} 1/K		
b_4	2.36×10^{-2}		

Using this procedure and the curve fits above, the PLIF images were converted into two-dimensional plots of naphthalene mole fraction. To reduce noise, a 3×3 median filter was applied to all images.

No correction was made for potential laser absorption by naphthalene vapor since negligible absorption was observed in the test cell over a distance larger than the boundary layer thickness in the current experiments.

PIV Image Processing

The raw PIV particle image pairs were processed in LaVision's DaVis software. The software recursively refined the interrogation window from 256×256 pixels to a final interrogation window of 64×64 pixels with a 50% overlap between interrogation windows. Given the magnification of approximately 8 μm/pixel, the final interrogation window had a physical size of approximately 512 μm and the resulting vector field had a size of 64×64 vectors. The number of spurious vectors removed by the DaVis software was less than 10% in all cases, and these missing vectors were interpolated using a nearest neighbor linear interpolation technique.

RESULTS

Instantaneous Naphthalene PLIF Images

Figure 3 is an instantaneous naphthalene PLIF image that has been normalized by the maximum signal in the image. The image has not been corrected for temperature and pressure effects using Equation 1. In all images shown here, the flow is depicted as moving from left to right. At this stage, the image is only qualitative although the fluorescence signal scales roughly with naphthalene concentration. This image is similar to those presented by Combs and Clemens (2015), however with a much higher signal-to-noise ratio, likely due to the increased quantum efficiency of the camera employed. In general, the signal appears to decrease with increasing distance from the wall in the y-direction and very little fluorescence signal is visible outside y/δ = 0.6. Using Rayleigh scattering, Smith et al. (1989) visualized similar large scale structures in a Mach 2.5 boundary layer out to distances of approximately y/δ = 0.8 while Baumgartner et al. (1997) observed these features beyond y/δ = 1 in a Mach 8 boundary layer. The structures in the current study do not extend as far out into the boundary layer since the scalar is introduced only a short distance upstream of the imaging location.

The image in Figure 3 was then converted into a two-dimensional field of naphthalene mole fraction using Equation 1, with the result shown in Figure 4. The magnitude of the calculated naphthalene mole fraction in the turbulent structures between $0 < y/\delta < 0.2$ is on the order of 5×10^{-4} with an uncertainty of ± 20%. This peak value of mole fraction is approximately 5% of the saturation mole fraction at the wind tunnel recovery temperature and static pressure ($\chi_{sat}(T) = P_{sat}(T)/P$, where the vapor pressure of naphthalene was calculated using data from De Kruif et al., 1981). This value is slightly higher than those observed by Combs and Clemens (2015) and is most likely caused by the higher wind tunnel stagnation temperature used in the current study (360 K in the current work compared to 350 K in Combs and Clemens, 2015).

Comparing Figure 3 and 4, the mole fraction field has many similarities with the uncorrected PLIF image. Relatively large-scale structures are still evident and the signal essentially vanishes by y/δ = 0.6. However, the subtle effect of the temperature and pressure correction is present, as well. For example, it seems that certain naphthalene vapor structures become more uniform in composition after the images have been converted to mole fraction. Two instances of this occurrence are indicated by white circles labelled "Naphthalene Vapor Structures" in Figure 4. When comparing the regions inside the white circles in Figure 4 to the same locations in Figure 3, one can see that scalar structures are more uniform in Figure 4. Without an instantaneous temperature correction, though, it is difficult to definitively say that these structures of uniform naphthalene mole fraction are present in the boundary layer.

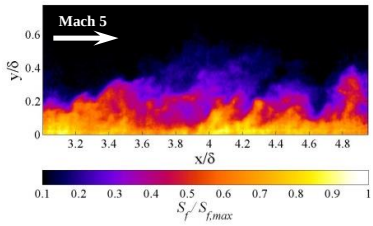

Figure 3. Normalized instantaneous naphthalene PLIF image in a Mach 5 turbulent boundary layer. Flow is from left to right.

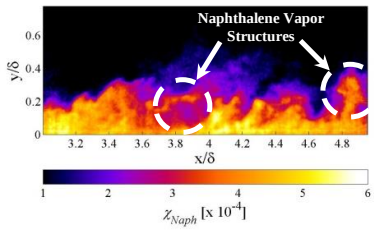

Figure 4. Instantaneous naphthalene mole fraction in a Mach 5 turbulent boundary layer. Flow is from left to right.

Simultaneous PIV and Naphthalene PLIF Images

Figure 5 presents some typical instantaneous fields of normalized naphthalene mole fraction paired with the simultaneously-acquired instantaneous streamwise and wall-normal velocity fields. The measured fluorescence

signal intensity was significantly lower when making simultaneous PIV measurements compared to runs where only PLIF images were collected. The cause of this is still under investigation, however, it is suspected that the PIV seed particles are either obscuring the camera's field of view or inhibiting the sublimation rate of the naphthalene insert by coating its surface. As this effect has been observed to worsen with successive runs, one possible future solution may be to clean the wind tunnel surfaces of TiO_2 residue prior to each run. Examining the images reveals that, in general, the regions with high naphthalene mole fraction tend to correspond with structures having a relatively low streamwise velocity component, u. Additionally, the naphthalene vapor structures again appear to be confined within $y/\delta < 0.6$ along with the regions of low streamwise velocity, similar to what was observed by Buxton et al. (2012). Meanwhile, a correlation with the wall-normal velocity component, v, is not as obvious with the fluctuations about zero appearing to be relatively disconnected from the scalar field.

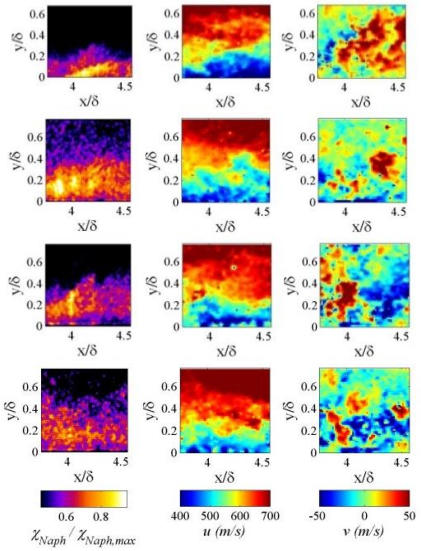

Figure 5. Typical instantaneous fields (rows) of normalized naphthalene mole fraction (left column) paired with simultaneously acquired streamwise (center column) and wall-normal (right column) velocity fields.

To further examine the relationship between scalar concentration and velocity, Figure 6 is presented, which shows the covariance, ρ, of the naphthalene mole fraction with both components of velocity, where

$$\rho_{x,y} = \frac{<(x-<x>)*(y-<y>)>}{\sigma(x)\sigma(y)} \qquad (4)$$

and $\sigma(x)$ is the standard deviation of x. The plot first comfirms the relationship between u and χ that is illustrated by the image sets in Figure 5, as negative fluctuations in u are shown to correspond with an increase in naphthalene mole fraction. This correlation reaches a peak between $0.3 < y/\delta < 0.4$, the outer edge of most of the naphthalene vapor structures. Buxton et al. (2012) noticed a similar peak at $y/\delta = 0.3$. Figure 6 also illuminates a correlation between v and χ, with increased naphthalene mole fraction appearing to coincide with positive fluctuations in v. As with the correlation with streamwise velocity, this correlation peaks between $0.3 < y/\delta < 0.4$. Combining these two pieces of information, it becomes evident that the naphthalene vapor structures present in the boundary layer are the result of an ejection mechanism, whereby fluid near the wall—traveling at relatively low streamwise velocity and containing a relatively high concentration of naphthalene vapor—is ejected out into the boundary layer by a turbulent burst with a relatively high wall-normal velocity component, as previously discussed by Robinson (1991) and Spina et al. (1994).

Furthermore, for $y/\delta < 0.2$ the covariance appears to be relatively small, but given the low signal-to-noise ratio of the PLIF data, this observation is not conclusive. However, the trends in the covariances near the wall ($\rho_{u'\chi}>0$; $\rho_{v'\chi}<0$), although noisy, were also observed by Buxton et al. (2012).

In addition to providing value in analyzing the correlation between scalar and velocity, the covariance values plotted are essentially a normalized version of the turbulent scalar fluxes that are essential to the computation of scalar transport. These profiles are similar to those presented in a computational study by Braman et al. (2011) for an ablating surface in a Mach 1.2 flow.

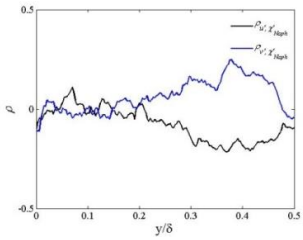

Figure 6. Plots of covariance between u' and χ'_{Naph} (black) and v' and χ'_{Naph} (blue) in the wall-normal direction.

Mean Scalar and Velocity Profiles

To further analyze the instantaneous results, 12 sequential PLIF images acquired during a single wind tunnel run at the same streamwise location were averaged. These mean two-dimensional fields of PLIF signal and mole fraction were then averaged in the x-direction, resulting in mean boundary layer profiles which are presented in normalized form in Figure 7. The mean boundary layer velocity profile from the current work that was used for determining the mean temperature field is plotted in Figure 7 as well. Looking at the one-dimensional profiles it is clear that the mean naphthalene mole fraction steadily decreases with increasing distance from the wall, as expected. This trend is quite similar in both the uncorrected and corrected profiles. By a wall distance of approximately $y/\delta = 0.5$ the naphthalene mole fraction is effectively zero, corresponding to the signal level observed in the images. When comparing the mean mole fraction profile to the mean velocity profile it is also clear that regions with large negative values of $\partial\chi_{Naph}/\partial y$ correspond to areas with relatively high $\partial u/\partial y$. The general trend of the scalar profile agrees with those measured previously by Poreh and Cermak (1964), Gross and McKenzie (1985), Carvin et al. (1988), and Fletcher

and McKenzie (1992). However, it is difficult to compare scalar profiles from the literature to the current case given that the scalar is seeded into a turbulent boundary layer that is already fully developed.

Lastly, Figure 8 is a comparison of the mean boundary layer profiles of naphthalene mole fraction and velocity plotted in wall units. Naphthalene mole fraction is presented as $1-<\chi_{Naph}>/\chi_{Naph,max}$ and the Van Driest transformation has been applied to the velocity profile. As seen in the figure, both profiles exhibit logarithmic behavior from $100 < y^+ < 300$ when compared to the law of the wall (Van Driest, 1951), similar to observations made by Carvin et al. (1988). Additionally, the profiles both appear to have a similar shape for the entire range of y^+ for which data was acquired.

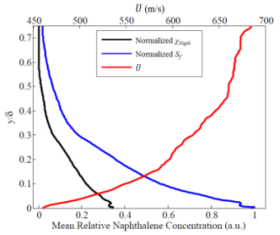

Figure 7. Comparison of normalized boundary layer profiles of fluorescence signal and naphthalene mole fraction. The mean velocity profile used in the current work is also plotted.

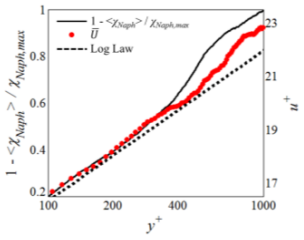

Figure 8. Profiles of $1-<\chi_{Naph}>/\chi_{Naph,max}$ and the Van Driest transformed mean streamwise velocity profile compared to the log law and plotted in normalized wall units.

CONCLUSIONS

Quantitative naphthalene PLIF was employed simultaneously with PIV to acquire simultaneous two-dimensional fields of naphthalene mole fraction and velocity. Large-scale naphthalene vapor structures out to wall distances of approximately $y/\delta = 0.6$ were revealed that coincide with regions of relatively low streamwise velocity. These turbulent structures between $0 < y/\delta < 0.2$ have a naphthalene mole fraction on the order of 5×10^{-4}, which is approximately 5% of the saturation mole fraction in the boundary layer, with a measurement uncertainty of ± 20%. It was demonstrated that regions of high scalar coincided with negative fluctuations in streamwise velocity and positive fluctuations in wall-normal velocity away from the wall, indicating that an ejection mechanism is transporting low-momentum, high-scalar-concentration fluid away from the wall (Robinson, 1991; Spina et al., 1994). Mean profiles of streamwise velocity and naphthalene mole fraction were also presented, with the mean mole fraction exhibiting its highest concentration near the wall and decaying to zero in the outer boundary layer. When plotted in wall units, the mean mole fraction and velocity profiles exhibited a logarithmic dependence on y^+ over $100 < y^+ < 300$.

ACKNOWLEDGEMENT

This work was supported by a NASA Office of the Chief Technologist's Space Technology Research Fellowship Grant (#NNX11AN55H).

REFERENCES

Braman, K., H. Koo, V. Raman, R. Upadhyay, and O. Ezekoye, AIAA paper 2011-207, *49th AIAA Aerospace Sciences Meeting*, 2011.

Buxton, O., B. Lochman, M. Sharma, and N. T. Clemens, AIAA Paper 2012-0440, *50th AIAA Aerospace Sciences Meeting*, 2012.

Carvin, C., J. F. Devieve, and A. J. Smits, AIAA Paper 88-0136, *26th AIAA Aerospace Sciences Meeting*, 1988.

Combs, C. S., N. T. Clemens, and P. M. Danehy, AIAA Paper 2014-1152, *52nd AIAA Aerospace Sciences Meeting*, 2014a.

Combs, C. S., N. T. Clemens, and P. M. Danehy, *17th International Symposia on Applications of Laser Techniques to Fluid Mechanics*, 2014b.

Combs, C. S. and N. T. Clemens, AIAA Paper 2015-1912, *53rd AIAA Aerospace Sciences Meeting*, 2015.

De Kruif, C. G., T. Kuipers, J.C. van Miltenburg, R.C.F. Schaake, and G. Stevens, *Journal of Chemical Thermodynamics*, Vol. 13, No. 11, 1981, pp. 1081-1086.

Fletcher, D. G. and R. L. McKenzie, *Optics Letters*, Vol. 17, No. 22, 1992, pp. 1614-1616.

Gross, K. P. and R. L. McKenzie, *AIAA Journal*, Vol. 23, No. 12, 1985, pp. 1932-1936.

Ho, D. W. K., Koo, J. H., Bruns, M. C., and Ezekoye, O. A., AIAA Paper 2007-5773, *43rd AIAA/ ASME/ SAE/ ASEE Joint Propulsion Conference & Exhibit*, 2007.

Hou, Y. X. 2003. Ph. D. Dissertation, The University of Texas at Austin.

Lochman, B. 2010. Master's Thesis, The University of Texas at Austin.

McClure, W. B. 1992. Ph. D. Dissertation, The University of Texas at Austin.

Poreh, M. and J. E. Cermak, *Int. Journal of Heat and Mass Transfer*, Vol. 7, 1964, pp. 1083-1095.

Robinson, S. K., *Annu. Rev. Fluid Mech.*, Vol. 23, 1991, pp. 601-639.

Samimy, M. and S. K. Lele, *Physics of Fluids*, Vol. 3, No. 8, 1991, pp. 1915-1923.

Smits, A. J., Martin, M. P., and Girimaji, S., AIAA Paper 2009-151, *47th AIAA Aerospace Sciences Meeting and Exhibit*, 2009.

Spina, E. F., A. J. Smits, and S. K. Robinson, *Annu. Rev. Fluid Mech.*, Vol. 26, 1994, pp. 287-319.

Stogner, R., P. T. Bauman, K. W. Schulz, R. Upadhyay, and A. Maurente, AIAA Paper 2011-764, *49th AIAA Aerospace Sciences Meeting and Exhibit*, 2011.

Van Driest, E. R., *Journal of Aeronautical Science*, Vol. 18, No. 3, 1951, pp. 145-160.